Check for updates

Terahertz-slicing — an all-optical synchronization for 4th generation light sources

M. CHEN,[1,2] T. V. A. G. DE OLIVEIRA,[1,3,4,7] I. ILYAKOV,[1] T. NÖRENBERG,[1,4] F. KUSCHEWSKI,[3,5] J.-C. DEINERT,[1] N. AWARI,[1] A. PONOMARYOV,[1] M. KUNTZSCH,[1] S. C. KEHR,[3] L. M. ENG,[3,4] M. GENSCH,[2,6] AND S. KOVALEV[1,8]

[1]*Helmholtz-Zentrum Dresden-Rossendorf, Bautzner Landstr. 400, 01328 Dresden, Germany*
[2]*Institut für Optik und Atomare Physik, Technische Universität Berlin, Strßae des 17. Juni 135, 10623 Berlin, Germany*
[3]*Institut für Angewandte Physik, Technische Universität Dresden, Nöthnitzer Str. 61, 01187 Dresden, Germany*
[4]*ct.qmat – Cluster of Excellence on Complexity and Topology in Quantum Matter, Dresden, Germany*
[5]*DLR - Institute of Quantum Technology, Wilhelm-Runge-Straße 13, 89081 Ulm, Germany*
[6]*DLR - Institute of Optical Sensor Systems, Rutherfordstr. 2, 12489 Berlin, Germany*
[7]*t.de-oliveira@hzdr.de*
[8]*s.kovalev@hzdr.de*

Abstract: A conceptually new approach to synchronizing accelerator-based light sources and external laser systems is presented. The concept is based on utilizing a sufficiently intense accelerator-based single-cycle terahertz pulse to slice a thereby intrinsically synchronized femtosecond-level part of a longer picosecond laser pulse in an electro-optic crystal. A precise synchronization of the order of 10 fs is demonstrated, allowing for real-time lock-in amplifier signal demodulation. We demonstrate successful operation of the concept with three benchmark experiments using a 4th generation accelerator-based terahertz light source, i.e. (i) far-field terahertz time-domain spectroscopy, (ii) terahertz high harmonic generation spectroscopy, and (iii) terahertz scattering-type scanning near-field optical microscopy.

1. Introduction

Achieving robust femtosecond level synchronization of modern accelerator-based light sources to ultrafast laser systems is, despite the tremendous progress over the past decade, still a fundamental challenge to exploit the full potential of large-scale photon science facilities such as XFELs. Many of the discussed breakthrough experiments, such as observing molecular movies or bond-breaking on the relevant time- and length-scales [1,2] or observing the highly nonlinear kinetics of charge carriers in quantum materials [3–5], etc. are depending on technological solutions that provide precise, femtosecond-level synchronization for extended periods of time (i.e., hours). In this letter, we introduce a new scheme that conceptually follows a fundamentally different route as compared to any other employed method to date. Instead of synchronizing the laser system and the accelerator to a highly precise external clock [6–8], or implementing active feedback loops to stabilize the laser pulse arrival time to that of the electron bunches in the linear accelerator [9], or implementing a *post-mortem* arrival time correction method [10–12], we show here that external laser pulses can also be passively synchronized to the electron bunch or accelerator-based radiation pulse, via the terahertz (THz)-slicing approach [13]. The key aspect of our scheme is that we use an ultra-short single-cycle THz pulse parasitically generated by the electron bunch (e.g., from a diffraction radiator [14]) to slice an intrinsically synchronized ultra-short portion from a conditioned few picosecond (ps) long laser pulse. The slicing of the laser pulse is achieved through the electro-optic (EO) effect in a suitable nonlinear optical crystal. Due to the parametric

origin of light-matter interaction in the EO crystal, the sliced portion of the pulse is intrinsically synchronized to the electron bunch.

The THz-slicing approach introduced here may be considered as the reverse process to the "femtoslicing" concept employed in synchrotron storage rings [15], which is used to generate few 10 fs X-ray pulses from few 10 ps long electron bunches, which are then synchronized to the "slicing" laser pulse. For "femtoslicing", femtosecond near-infrared laser pulses are utilized to impose an fs energy modulation onto the ps-to-ns long electron bunch. By doing so, the near-infrared femtosecond laser is then intrinsically synchronized to the femtosecond XUV/X-ray light pulses generated from the modulated portion of the electron bunch. The fundamental difference between "femtoslicing" and our scheme is that the THz-slicing method achieves this synchronization by slicing a long near-infrared laser pulse via interaction with a THz pulse, generated from the electron bunches, in an EO crystal. Our concept is hence all-optical and does not require any interaction between the electron bunches and the fs laser pulses. For this reason, the unperturbed electron bunch can be further used for other secondary radiation sources, while the sliced optical pulse will be synchronized to them passively.

In this letter, the performance of the THz-slicing is characterized, and its applicability is demonstrated at the superradiant THz facility TELBE [16]. It is shown that timing instabilities can be compensated by two orders of magnitude, reaching a few ten-femtosecond synchronization level even when the initial timing jitter is up to 4 ps (RMS). Three experiments: linear far-field THz time-domain spectroscopy (THz-TDS), THz high harmonic generation (THz HHG) spectroscopy, and THz scattering-type scanning near-field optical microscopy (THz s-SNOM) are performed to benchmark the concept.

2. Experimental setups

2.1. THz-slicing method

The experiments were performed at the ELBE Center for High-Power Radiation Sources and the associated superradiant THz facility TELBE located at Helmholtz-Zentrum Dresden-Rossendorf (HZDR). The superconducting linear accelerator at ELBE provides highly compressed electron bunches of ~200 fs (RMS) bunch duration and 26 MeV bunch kinetic energy at a repetition rate of 250 kHz [17]. Single and multicycle THz pulses are generated by two sources, a coherent diffraction radiator (CDR) and an electromagnetic undulator. A schematic overview of the THz radiators in conjunction with the experimental setups for all three types of benchmark experiments is presented in Fig. 1. In the experimental setups, the CDR source typically emits temporally short single-cycle THz pulses that are used as gate pulses for the THz-slicing module, while the multicycle pulses from the undulator source are used to perform the benchmark experiments as described below. Both CDR and undulator pulses are generated in the regime of superradiant emission from the same electron bunch and hence are intrinsically synchronized and carrier-envelope-phase (CEP) stable [16]. The residual timing jitter between these two sources is typically below 10 fs (RMS) [18].

A table-top Ti:sapphire amplified laser system (Coherent Inc. RegA) operated at the same repetition rate as the accelerator (250 kHz) is utilized in all experiments presented, which provided 35 fs (FWHM) pulses centered at a wavelength of 800 nm. This laser is coarsely synchronized with the ELBE accelerator through a commercial system called Synchrolock-AP [19] using a RF clock with controllable laser-to-undulator pulse timing jitter, adjustable between 500 fs to 4 ps (RMS). In the THz-slicing module, the 35 fs (FWHM) laser pulses are stretched in time to a duration of 1.2 ps (FWHM) by passing through a 150-mm-long highly dispersive N-SF6 glass rod (see blue curve in Fig. 2(a)). The stretched laser pulse and the CDR THz pulse are then copropagated through a (110) ZnTe crystal. The linearly polarized CDR THz pulses are focused to a spot size of 1 mm in diameter and have an average pulse energy of 240 nJ. Given that the two pulses are overlapped in time, a polarization modulation of the portion of the laser
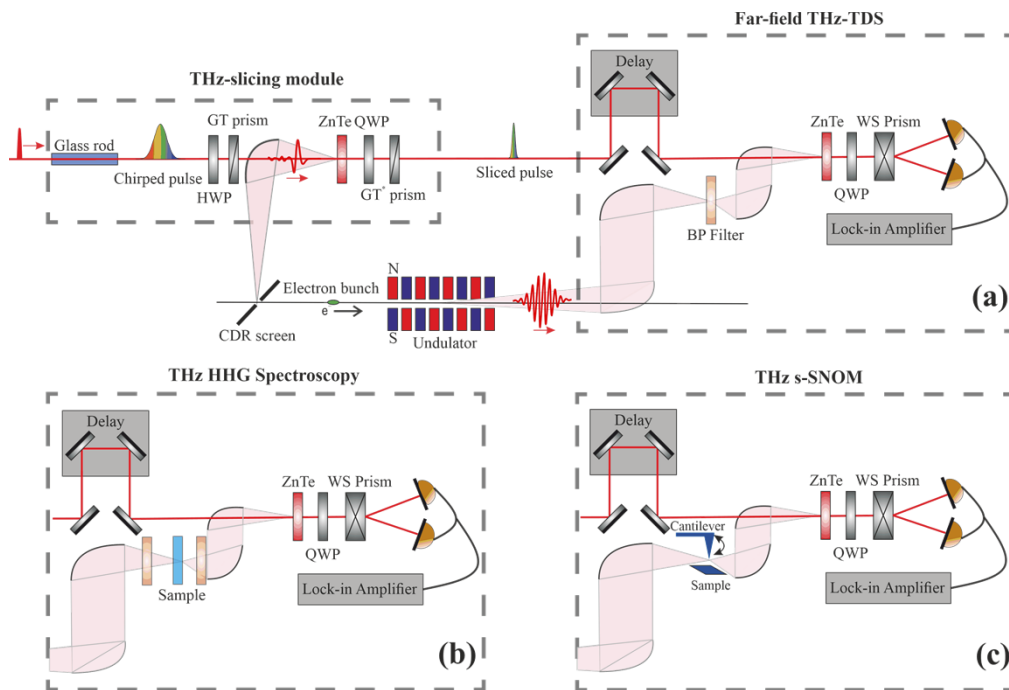
Fig. 1. Experimental setup of the THz time-domain spectroscopy experiment using THz-slicing technology in conjunction with superradiant THz sources. The dashed boxes indicate the THz-slicing module and the different ultrafast experimental schemes: far-field THz-TDS in (a), time-domain THz HHG in (b) and time-domain THz s-SNOM in (c). In the THz-slicing module, a glass rod is used to stretch the laser pulse. The CDR and the stretched pulse interact in the ZnTe crystal, while the half-wave plate (HWP) and the GT prisms are set to a cross-polarized arrangement. The synchronously sliced pulse is directed to the ultrafast experiments as probe pulse. (a) In the far-field THz-TDS scheme, the multicycle THz pulse is focused on a 2 mm thick ZnTe crystal and is characterized by EO sampling. (b) In the time-domain THz HHG scheme, the multicycle THz pulse is focused onto the sample, with two BP filters introduced in front and behind the sample. The generated THz higher harmonics are then again characterized by EO sampling in a 2 mm thick ZnTe crystal. (c) In the time-domain THz s-SNOM scheme, the multicycle THz pulse is focused onto the sample area underneath the oscillating cantilever tip of the near-field microscope and the scattered THz radiation is measured by EO sampling in a 2 mm thick ZnTe crystal. The weak near-field contribution is distinguished from the huge far-field background by demodulation techniques.

pulse overlapped with the comparatively short THz pulse from the CDR radiator is achieved by the electro-optic effect. Two Glan-Taylor (GT) polarizers are oriented in a cross-polarization arrangement and are placed at either side of the ZnTe crystal, ensuring that only this "sliced" part of the laser pulse is transmitted. The theoretical background and optimal configuration for this process, coined THz-slicing, are described in Ref. [13]. The sliced pulses were characterized by measuring their spectrum and pulse duration with a grating spectrometer and an intensity auto-correlator.

Three different benchmark experiments were performed combining the sliced NIR pulses with the THz pulses from the undulator: (i) linear far-field THz time-domain spectroscopy (THz-TDS) (ii) THz high harmonic generation (THz HHG) spectroscopy, and (iii) THz scattering-type scanning near-field optical microscopy (THz s-SNOM).
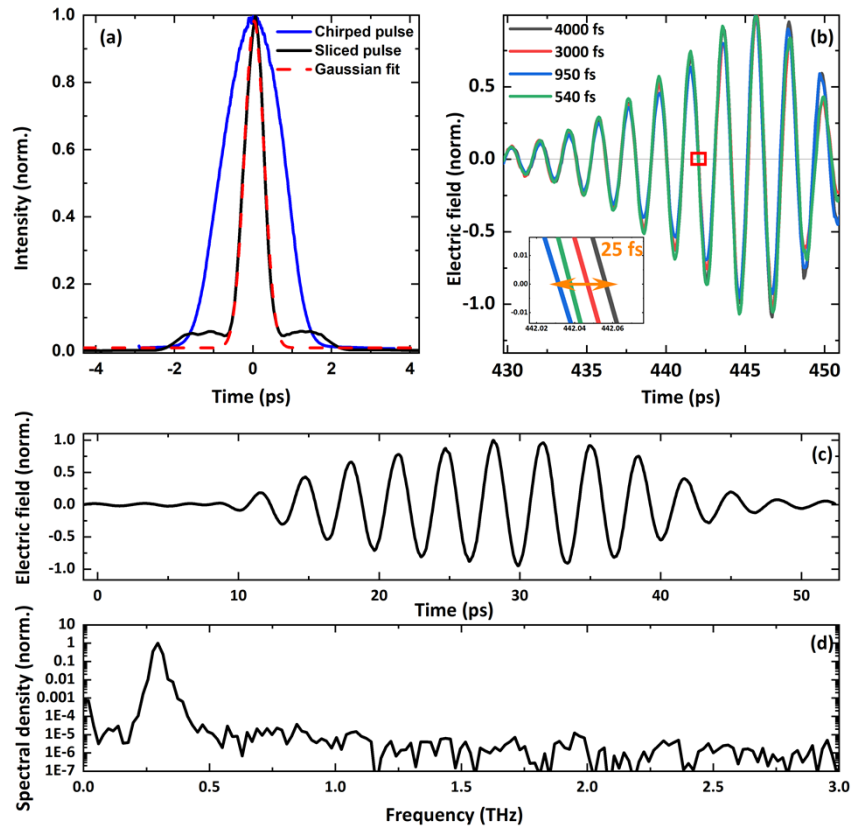
Fig. 2. (a) Autocorrelation function of the stretched pulse (solid blue curve), sliced pulse (solid black curve), and a Gaussian fit (dashed red curve). (b) Part of the THz waveforms of undulator pulses measured for different levels of timing jitter adjusted by the setting of the Synchrolock device. Inset: The zoom-in view of the red rectangular area at one zero-crossing position. (c) Full THz waveform and (d) spectrum of undulator pulses at 300 GHz. Measurements were performed through a band pass filter centered around 300 GHz.

2.2. Linear far-field THz time-domain spectroscopy (THz-TDS)

In the far-field THz-TDS, as shown in Fig. 1(a), the sliced pulse generated by the THz-slicing module is directly used as probe pulse in the EO sampling detection with a ZnTe crystal (2 mm). Standard EO sampling, utilizing a quarter-wave plate (QWP), Wollaston prism (WP), and balanced photodetectors is utilized. A bandpass (BP) filter is put at the focus of the multicycle THz radiation, allowing only the fundamental frequency of the superradiant undulator source to pass.

2.3. THz high harmonic generation (THz HHG) spectroscopy

In the THz HHG spectroscopy experiment, the sliced pulse is also used as a probe pulse in the EO sampling detection scheme, as shown in Fig. 1(b). The sample is placed at the focus of the multicycle THz radiation with two bandpass filters positioned in front and behind the sample, to allow the excitation of the sample with the THz fundamental frequency and to enable higher detection sensitivity of the THz high harmonic frequency generated by the sample [3].

2.4. *THz scattering-type scanning near-field optical microscopy (THz s-SNOM)*

For the THz s-SNOM experiment, a home-built s-SNOM operated in forward-scattering geometry was utilized, as shown schematically in Fig. 1(c). The THz undulator pulse is focused onto the tip using a 2" off-axis parabolic (OAP) mirror with a focal length of 75 mm, while the near-field signal is collected using another high numerical aperture OAP mirror with a focal length of 50 mm positioned at the opposite side of the tip. Detection was done by electro-optic sampling using the sliced laser pulse in a 2 mm thick ZnTe crystal. Commercially available metallic tips were used (Rocky Mountain Nanotechnology, LLC, Model 25PtIr300B), possessing a natural resonance frequency Ω of around 20 kHz and a tip radius of approximately 20 nm. The tip oscillation frequency was chosen to be sufficiently smaller than the repetition rate of the THz source of 250 kHz. Sample positioning and scanning were done with Attocube stages (Px101, Pz101, ANSxyz50), while the whole system was controlled by an RHK R9 scanning probe microscopy controller.

3. Results

Before performing the benchmark experiments, the properties of the sliced laser pulses were characterized. The autocorrelation measurements of the initial chirped pulse and the THz sliced pulse are displayed in Fig. 2(a). The pulse duration and the shape of the sliced pulse strongly depend on the QWP and the GT orientations in use [13]. By optimizing the orientation of the QWP and the GT prisms, the minimal duration of the sliced pulse measured approximately 350 fs (FWHM) that is mainly limited by the CDR pulse duration, which, in turn, depends on the electron bunch length and the aperture size of the used CDR screen [16,20]. THz-sliced pulses with energy of about 16 nJ starting from a chirped laser pulse of 6.3 µJ are obtained, corresponding to a 0.25% conversion efficiency. Note that a residual component (< 1.5 nJ) of the chirped pulse still leaks in the THz-slicing process, giving rise to the shoulders observed in the autocorrelation measurements of Fig. 2(a).

3.1. *Far-field THz-TDS*

The main advantage of the THz-slicing approach is the possibility of passively compensating the timing jitter between accelerator and laser. The passive compensation via nonlinear optics means that the sliced pulse is intrinsically synchronized to the accelerator, while its performance does not depend on the level of the initial timing jitter between these two sources. At such conditions, standard heterodyne detection techniques, such as the use of lock-in amplifiers, can be employed directly without signal or temporal resolution losses even when employing long integration times.

To demonstrate the immunity of the THz-slicing technique against the initial timing jitter, we measured the temporal THz waveform of the undulator radiation under different initial accelerator-to-laser jitter conditions, ranging from 0.5 to 4 ps (RMS) (see Fig. S5 in the supplementary material). These measurements were performed with standard EO sampling using a lock-in amplifier operating at 700 Hz demodulation frequency (see Fig. S2 in the supplementary material for the experimental setup). The undulator beam was modulated at this frequency with a mechanical chopper.

THz waveforms of the undulator pulse measured under various jitter levels are shown in Fig. 2(b). While the inset shows the enlarged area at one "zero-field" position of multiple traces measured at different jitter levels recorded over the course of 1 hour. We observe that even with temporal jitters as large as 4 ps the detected THz waveforms show only marginal phase shifts, indicating that THz-sliced near-infrared pulses are indeed synchronized to the THz pulses emitted from the undulator. Figure 2(c) shows the full THz waveform of the undulator pulse tuned to 300 GHz and sampled over 50 ps. Figure 2(d) shows the corresponding intensity spectrum. A spectral dynamic range of 10^6 and a time-domain signal-to-noise ratio (SNR) on the order of 10^4

(see supplementary material for details) is demonstrated for an integration time of 300 ms per data point.

The EO sampling measurements shown in Fig. 2(c) were performed at about 500 fs (RMS) initial timing jitter. At such conditions, EO sampling *without* the THz-slicing approach (using initial 35 fs laser pulses as probe) yields measurements with extremely poor SNR, which is further corrupted by slow thermally-induced timing drifts (see Figure S6 in supplementary material). The conservative estimation for the upper limit of the pulse-to-pulse residual timing jitter between THz-sliced pulse and accelerator is < 44 fs (RMS) (see Note 1c and Figure S4 in supplementary material).

### 3.2. THz HHG from a grating-graphene metamaterial

In addition to linear THz-TDS, a benchmark experiment was performed to demonstrate the performance of the THz-slicing method in a nonlinear THz spectroscopy experiment. Thereby it is demonstrated that THz-slicing can be utilized in experiments that require the detection of extremely low THz intensities. The chosen example experiment is the generation of THz higher harmonics in a grating-graphene metamaterial. The experiment had previously been successfully performed at the TELBE facility by employing a pulse-resolved arrival time correction scheme [3,21]. In the experiment it was demonstrated that the grating-graphene metamaterial exhibits an exceptionally high conversion efficiency for generating THz harmonics owing to the characteristic carrier dynamics in the Dirac-type electronic band structure [22–24] combined with the field enhancement provided by specifically designed metallic stripe antennas [21]. The experimental setup is shown in Fig. 1(b).

The spectra of the generated 3rd harmonic under various fundamental pump field strengths (shown as a percentage with respect to full power) measured using the THz-slicing approach are shown in Fig. 3. The maximum pump field strength (shown as 100% in Fig. 3) corresponds to 13 kV/cm in free-space. Time-domain traces of the third harmonic generation (THG) and more details of the experiment are shown in the supplementary material.

The normalized THG peak field strength is plotted as a function of the normalized fundamental peak field strength on a double logarithmic scale (see the inset of Fig. 3). A nonlinear relationship can be extracted from the slope, indicating that the experiment was performed in the so-called saturation regime where the absorption saturation limits the energy transfer. The result is comparable to the results obtained by the conventional pulse-resolved *post-mortem* arrival time correction method from the same metamaterial [12,21], where it was shown that saturation is already reached for incident field strengths of < 10 kV/cm [21].

3.3. THz s-SNOM with intense THz radiation

s-SNOM is a unique nanoimaging technique that enables wavelength-independent spatial resolution over a wide spectral range, from visible to THz and even microwaves [25,26]. As such, the technique has been widely adopted at large-scale facilities, such as ultra-broadband synchrotron sources [27,28] and widely-tunable narrowband free-electron-laser sources [29–31]. In s-SNOM, a metallic or metalized tip oscillates in close proximity to the sample surface, wherein both tip and sample are illuminated by the light source of choice. The tip can act as a broadband antenna, concentrating the electric fields at its apex, or conversely, act as a highly localized dipole scatterer for the evanescent near-fields of a sample volume. The tip oscillation modifies the tip-sample near-field interaction, thus modulating the near-field signal scattering in time. As the near-field signal scattering has a highly nonlinear dependence on the tip-sample distance, the scattered signals are composed of multiple harmonics of the tip frequency ($n\Omega$, wherein n = 1, 2, 3…). As the far-field background signal is linearly modulated, demodulation of the scattered signals is done at a higher harmonic of the tip oscillation frequency (n ≥ 2), effectively suppressing the much larger far-field background contribution [32].
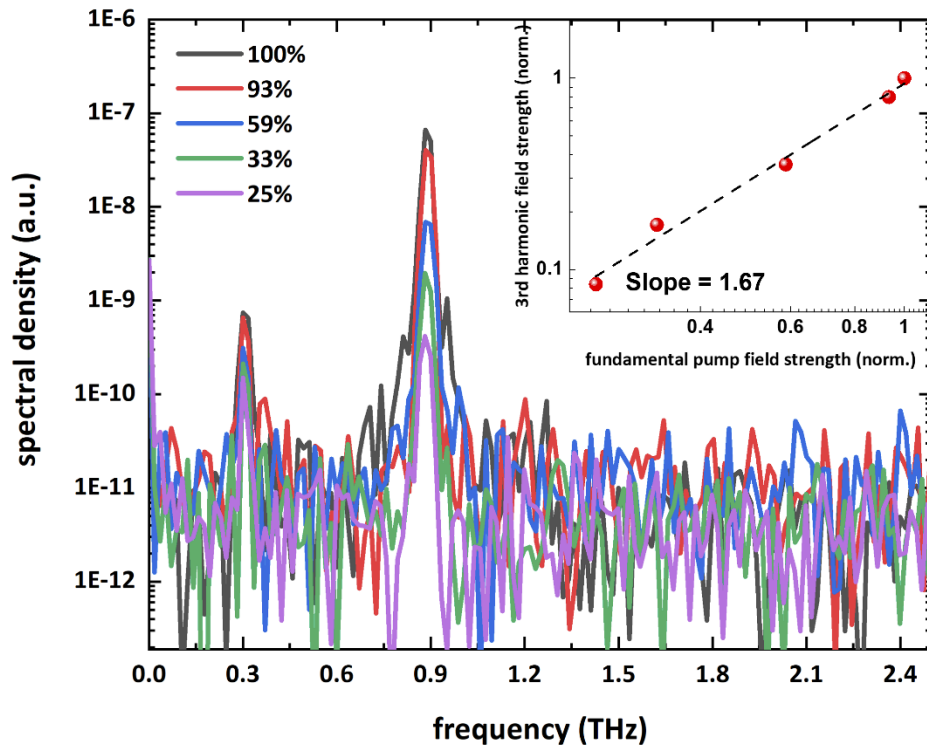
Fig. 3. Normalized spectra of the 3rd harmonic signal under different pump field strength with a 900 GHz bandpass filter placed right behind the sample. The maximum pump field strength (shown as 100% in Fig. 3) corresponds to 13 kV/cm. Inset: THG field strength plotted as a function of the fundamental pump field strength. A linear fit with a slope of 1.67 can be deduced from the logarithmic scale plot.

Recently, nanoimaging in the THz regime with s-SNOM has seen tremendous progress [33–38] using various table-top THz sources. In the context of pulsed THz sources, which are paramount to exploring the dynamics of THz-driven phenomena, near-field microscopy has been limited by the lack of sources of high spectral brightness, with currently available THz pulse energies reaching only a few tens of picojoules. While such a pulse energy level has proven to be sufficient for THz nanoimaging, it precludes the investigation of dynamics induced by intense THz transients [39,40], and, importantly, it also hinders the development of nonlinear nanoimaging methods [41] at THz frequencies.

Here we combine s-SNOM with the spectrally bright THz pulses from the undulator of the TELBE facility to demonstrate time-resolved near-field nanoimaging using intense narrowband THz radiation, with pulse energies reaching up to 10 nJ. This technological breakthrough is enabled by the THz-slicing technique, which, crucially, allowed real-time signal demodulation of near-field signals directly with a standard lock-in amplifier. By detecting the near-field signatures with the THz time-domain technique at room temperature, we demonstrate imaging with intense THz transients resolved in time, field, and at a significantly sub-wavelength spatial resolution. Note that although multi-nJ to μJ-level THz transients can be readily generated with table-top amplified mJ-level fs-laser systems, such sources typically operate at repetition rates < 5 kHz, which, without applying complex *post-mortem* signal reconstruction methods [42], precludes

s-SNOM operation. Also note that the few-nJ pulse energy level is chosen only for this specific s-SNOM experiment, while the highest achievable pulse energy can reach a few μJ.

In order to verify that near-field signatures can be extracted by employing the THz-slicing technique, we perform EO sampling measurements of the near-field signals scattered from a highly reflective gold sample surface (200 nm thick Au deposited on a Si substrate) upon excitation with 900 GHz radiation from TELBE's undulator source. To this end, we demodulate the EO sampling signal at the n-th harmonic of the cantilever tapping frequency, as shown in Fig. 4. As expected for s-SNOM, the near-field signal amplitude decays rapidly with demodulation order. The spectral dynamic range is approximately 10^3 for the 2Ω near-field signal integrated over 300 ms, which is only slightly worse than what is obtained when using table-top, low-noise THz sources [43]. This is expected as here the THz undulator is operated at a comparably low 250 kHz repetition rate. At such modest repetition rates, the sampling rate of the cantilever oscillation is much lower than for oscillator-based THz sources operating at multi-MHz repetition rates.
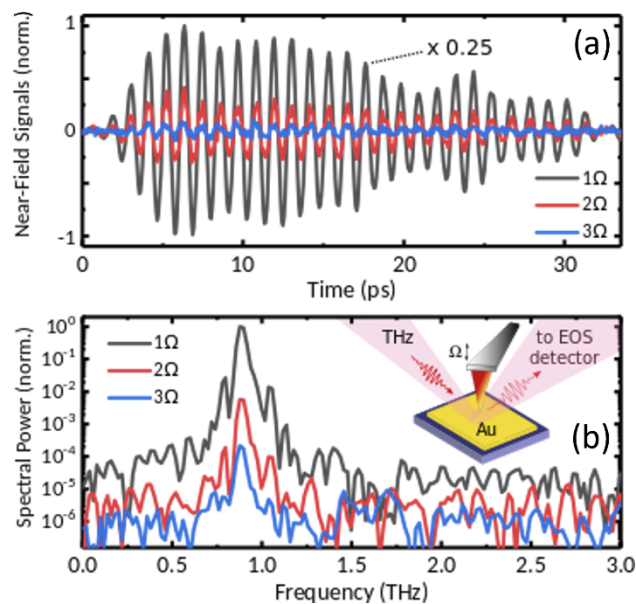

Fig. 4. THz s-SNOM near-field signals from an Au sample. (a) THz waveforms demodulated at Ω, 2Ω, and 3Ω, and (b) their corresponding power spectra. The inset in (b) shows a sketch of the THz s-SNOM experiment on the 200 nm thick patterned Au structures on a silicon substrate.

To demonstrate the time-domain THz nanoimaging capabilities of the instrument, we recorded the scattered near-field signals for a structured sample, as shown in Fig. 5. In order to obtain a surface showing a different permittivity than its supporting substrate, in addition to having sub-micrometer geometry naturally, we have exfoliated the topological insulator (TI) n-doped Bi_2Se_3 (2D Semiconductors, USA) on a THz-transparent high-resistivity silicon substrate. As a result, we obtained μm-sized TI flakes of a metallic character, as the Fermi level of Bi_2Se_3 lies within the bulk conduction bands [44].

For imaging, the sample is raster-scanned under the s-SNOM tip, while the topography and the scattered THz waveforms are recorded simultaneously (see Fig. 5(a)). The evolution of the scattered near-field $NF_{2\Omega}$ is measured in the time-domain for Bi_2Se_3 and for the Si substrate and are shown in Fig. 5(c). The topography image of the selected 190 nm thick Bi_2Se_3 flake is shown in Fig. 5(b). A multicycle scattered near-field for the narrowband 900 GHz excitation is observed,
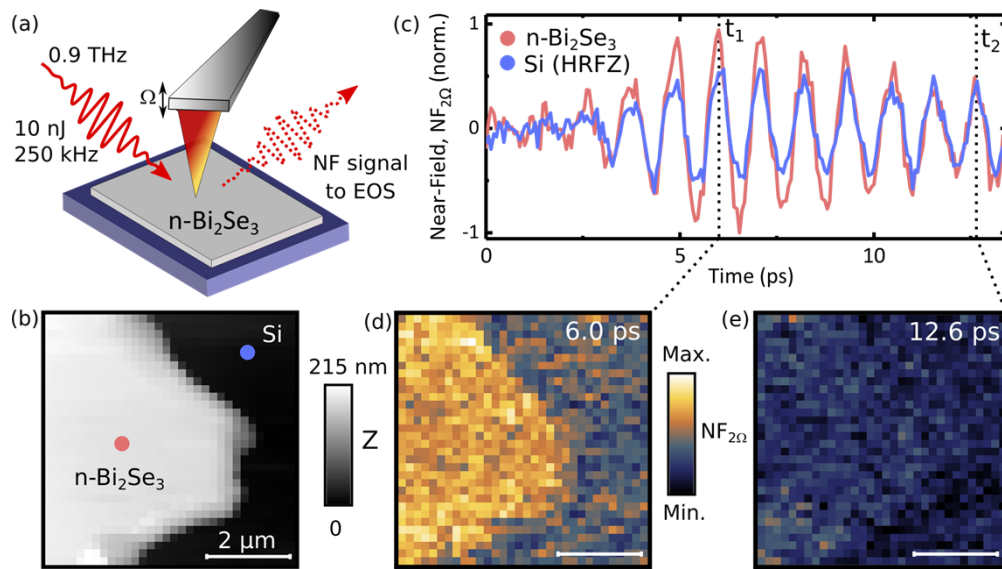
Fig. 5. THz s-SNOM of a topological insulator (TI) n-Bi$_2$Se$_3$ flake deposited onto a high-resistivity float-zone silicon substrate in the time-domain. (a) Schematic of the THz s-SNOM set-up; (b) topography image of the studied 190 nm thick n-Bi$_2$Se$_3$ flake. (c) Time-domain near-field responses recorded on both the Si substrate (blue) and the TI flake (red) when applying the THz-slicing technique. Two dashed lines indicate the time delay of $t_1 = 6.0$ ps and $t_2 = 12.6$ ps, respectively; (d,e) near-field images NF$_{2\Omega}$(x, y, t) recorded for t equal (d) 6.0 ps and (e) 12.6 ps, respectively.

with substantially higher signal amplitude (higher THz reflectivity) for the Bi$_2$Se$_3$ flake and no noticeable phase shifts.

In contrast to typical s-SNOM experiments, where the time-integrated near-field intensity is recorded, our experimental data correspond to snapshots of the electric near-fields taken at a fixed point in time, as defined by the THz-sliced NIR probe pulses used in EO sampling. Therefore, the image contrast observed in these near-field images is highly dependent on the relative time between THz pump and NIR probe pulses. To demonstrate such a time-dependent image formation after excitation with narrowband THz pulses, we recorded near-field images NF$_{2\Omega}$(x, y, t) at different relative probe delay times of $t_1 = 6$ ps and $t_2 = 12.6$ ps, as shown in Fig. 5(d),(e), respectively. A clear material contrast is observed between the Bi$_2$Se$_3$ flake and the substrate at t_1, while it nearly vanishes later at t_2, where the measured scattered near fields (for both materials) are at a peak position of the multicycle waveform. While a careful investigation of the origin of such a vanishing contrast has not been carried out in the current work, it is understood that extrinsic parameters, beyond the local dielectric properties of the material underneath the tip, may strongly affect the observed near-field signal amplitude at THz frequencies. The appearance of halos around metal structures [38], structural size-dependent contrast [36,45], the emergence of replicas of the scattered near-field waveform dependent on the length of the metallic cantilevers [46], are all among the interesting experimental observations reported so far.

4. Conclusions

We have demonstrated that all-optical femtosecond synchronization between a 4th generation accelerator-based light source and an external laser system can be achieved by the THz-slicing technique. THz-slicing enabled synchronization with timing jitter levels of few tens of femtosecond for an extended time, even when temporal instabilities between accelerator and laser measured up to 4 ps. The high SNR (10^4) and high dynamic range (10^6) achieved in THz-TDS measurements have enabled its applicability also for nonlinear THz spectroscopy measurements. Moreover, the method enabled the first successful demonstration of a THz s-SNOM in the context of a superradiant THz facility, opening up opportunities for future investigations of nonlinear THz-driven processes at the nanoscale. In the current configuration, the sliced pulse duration of 350 fs (FWHM) is still relatively long and primarily dictated by the electron bunch duration. The THz-slicing concept is also readily applicable to 4th generation lightsources working in the VUV or X-ray regime as also here the prerequisite of ultra-short, sufficiently charged electron bunches is fulfilled. At 4th generation XUV/X-ray light source facilities such as FLASH [47], LCLS [48], FERMI [49], where parasitic THz sources for diagnostics already exist [18,50,51], the bunch duration can be as short as 10 fs. In this case, substantially improved temporal resolution can be envisioned.

Supplemental document. See Supplement 1 for supporting content.

References

1. I. Inoue, Y. Deguchi, B. Ziaja, T. Osaka, M. M. Abdullah, Z. Jurek, N. Medvedev, V. Tkachenko, Y. Inubushi, H. Kasai, K. Tamasaku, T. Hara, E. Nishibori, and M. Yabashi, "Atomic-Scale Visualization of Ultrafast Bond Breaking in X-Ray-Excited Diamond," Phys. Rev. Lett. **126**(11), 117403 (2021).
2. M. Wagstaffe, L. Wenthaus, A. Dominguez-Castro, S. Chung, G. D. Lana Semione, S. Palutke, G. Mercurio, S. Dziarzhytski, H. Redlin, N. Klemke, Y. Yang, T. Frauenheim, A. Dominguez, F. Kärtner, A. Rubio, W. Wurth, A. Stierle, and H. Noei, "Ultrafast Real-Time Dynamics of CO Oxidation over an Oxide Photocatalyst," ACS Catal. **10**(22), 13650–13658 (2020).
3. H. A. Hafez, S. Kovalev, J. C. Deinert, Z. Mics, B. Green, N. Awari, M. Chen, S. Germanskiy, U. Lehnert, J. Teichert, Z. Wang, K. J. Tielrooij, Z. Liu, Z. Chen, A. Narita, K. Müllen, M. Bonn, M. Gensch, and D. Turchinovich, "Extremely efficient terahertz high-harmonic generation in graphene by hot Dirac fermions," Nature **561**(7724), 507–511 (2018).
4. S. Kovalev, K.-J. Tielrooij, J.-C. Deinert, I. Ilyakov, N. Awari, M. Chen, A. Ponomaryov, M. Bawatna, T. V. A. G. de Oliveira, L. M. Eng, K. A. Kuznetsov, G. K. Kitaeva, P. I. Kuznetsov, H. A. Hafez, D. Turchinovich, and M. Gensch, "Terahertz signatures of ultrafast Dirac fermion relaxation at the surface of topological insulators at room temperature," npj Quantum Mater. **6**(1), 84 (2021).
5. H. Chu, M. J. Kim, K. Katsumi, S. Kovalev, R. D. Dawson, L. Schwarz, N. Yoshikawa, G. Kim, D. Putzky, Z. Z. Li, H. Raffy, S. Germanskiy, J. C. Deinert, N. Awari, I. Ilyakov, B. Green, M. Chen, M. Bawatna, G. Cristiani, G. Logvenov, Y. Gallais, A. V. Boris, B. Keimer, A. P. Schnyder, D. Manske, M. Gensch, Z. Wang, R. Shimano, and S. Kaiser, "Phase-resolved Higgs response in superconducting cuprates," Nat. Commun. **11**(1), 6–11 (2020).
6. J. Kim, J. A. Cox, J. Chen, and F. X. Kärtner, "Drift-free femtosecond timing synchronization of remote optical and microwave sources," Nat. Photonics **2**(12), 733–736 (2008).

7. S. Schulz, I. Grguraš, C. Behrens, H. Bromberger, J. T. Costello, M. K. Czwalinna, M. Felber, M. C. Hoffmann, M. Ilchen, H. Y. Liu, T. Mazza, M. Meyer, S. Pfeiffer, P. Predki, S. Schefer, C. Schmidt, U. Wegner, H. Schlarb, and A. L. Cavalieri, "Femtosecond all-optical synchronization of an X-ray free-electron laser," Nat. Commun. **6**(1), 5938 (2015).
8. J. M. Byrd, L. Doolittle, G. Huang, J. W. Staples, R. Wilcox, J. Arthur, J. Frisch, and W. White, "Femtosecond synchronization of laser systems for the LCLS," in *Proceedings of International Particle Accelerator Conference* (2010), pp. 58–60.
9. K. Şafak, M. Xin, P. T. Callahan, M. Y. Peng, and F. X. Kärtner, "All fiber-coupled, long-term stable timing distribution for free-electron lasers with few-femtosecond jitter," Struct. Dyn. **2**(4), 041715 (2015).
10. M. Harmand, R. Coffee, M. R. Bionta, M. Chollet, D. French, D. Zhu, D. M. Fritz, H. T. Lemke, N. Medvedev, B. Ziaja, S. Toleikis, and M. Cammarata, "Achieving few-femtosecond time-sorting at hard X-ray free-electron lasers," Nat. Photonics **7**(3), 215–218 (2013).
11. M. Diez, A. Galler, S. Schulz, C. Boemer, R. N. Coffee, N. Hartmann, R. Heider, M. S. Wagner, W. Helml, T. Katayama, T. Sato, T. Sato, M. Yabashi, and C. Bressler, "A self-referenced in-situ arrival time monitor for X-ray free-electron lasers," Sci. Rep. **11**(1), 3562 (2021).
12. S. Kovalev, B. Green, T. Golz, S. Maehrlein, N. Stojanovic, A. S. Fisher, T. Kampfrath, and M. Gensch, "Probing ultra-fast processes with high dynamic range at 4th-generation light sources: Arrival time and intensity binning at unprecedented repetition rates," Struct. Dyn. **4**(2), 024301 (2017).
13. M. Chen, S. Kovalev, N. Awari, Z. Wang, S. Germanskiy, B. Green, J.-C. Deinert, and M. Gensch, "Towards femtosecond-level intrinsic laser synchronization at fourth generation light sources," Opt. Lett. **43**(9), 2213 (2018).
14. A. P. Potylitsyn, "Smith-Purcell effect as resonant diffraction radiation," Nucl. Instrum. Methods Phys. Res., Sect. B **145**(1-2), 60–66 (1998).
15. R. W. Schoenlein, S. Chattopadhyay, H. H. W. Chong, T. E. Glover, P. A. Heimann, C. V. Shank, A. A. Zholents, and M. S. Zolotorev, "Generation of Femtosecond Pulses of Synchrotron Radiation," Science **287**(5461), 2237–2240 (2000).
16. B. Green, S. Kovalev, V. Asgekar, G. Geloni, U. Lehnert, T. Golz, M. Kuntzsch, C. Bauer, J. Hauser, J. Voigtlaender, B. Wustmann, I. Koesterke, M. Schwarz, M. Freitag, A. Arnold, J. Teichert, M. Justus, W. Seidel, C. Ilgner, N. Awari, D. Nicoletti, S. Kaiser, Y. Laplace, S. Rajasekaran, L. Zhang, S. Winnerl, H. Schneider, G. Schay, I. Lorincz, A. A. Rauscher, I. Radu, S. Mährlein, T. H. Kim, J. S. Lee, T. Kampfrath, S. Wall, J. Heberle, A. Malnasi-Csizmadia, A. Steiger, A. S. Möller, M. Helm, U. Schramm, T. Cowan, P. Michel, A. Cavalleri, A. S. Fisher, N. Stojanovic, and M. Gensch, "High-field high-repetition-rate sources for the coherent THz control of matter," Sci. Rep. **6**(1), 22256 (2016).
17. J. Teichert, A. Arnold, G. Ciovati, J.-C. Deinert, P. Evtushenko, M. Justus, J. M. Klopf, P. Kneisel, S. Kovalev, M. Kuntzsch, U. Lehnert, P. Lu, S. Ma, P. Murcek, P. Michel, A. Ryzhov, J. Schaber, C. Schneider, R. Schurig, R. Steinbrück, H. Vennekate, I. Will, and R. Xiang, "Successful user operation of a superconducting radio-frequency photoelectron gun with Mg cathodes," Phys. Rev. Accel. Beams **24**(3), 033401 (2021).
18. F. Tavella, N. Stojanovic, G. Geloni, and M. Gensch, "Few-femtosecond timing at fourth-generation X-ray light sources," Nat. Photonics **5**(3), 162–165 (2011).
19. "Coherent Inc., Synchrolock-AP," https://www.coherent.com/assets/pdf/Sychrolock-AP-Data-Sheet.pdf.
20. S. Casalbuoni, B. Schmidt, and P. Schmüser, "Far-Infrared Transition and Diffraction Radiation Part I: Production, Diffraction Effects and Optical Propagation," TESLA Rep. **15**, 1–41 (2005).
21. J.-C. Deinert, D. A. Iranzo, R. Perez, X. Jia, H. A. Hafez, I. Ilyakov, N. Awari, M. Chen, M. Bawatna, A. N. Ponomaryov, S. Germanskiy, M. Bonn, F. H. L. Koppens, D. Turchinovich, M. Gensch, S. Kovalev, and K.-J. Tielrooij, "Grating-graphene metamaterial as a platform for terahertz nonlinear photonics," ACS Nano **15**(1), 1145–1154 (2021).
22. K. S. Novoselov, A. K. Geim, S. V. Morozov, D. Jiang, M. I. Katsnelson, I. V. Grigorieva, S. V. Dubonos, and A. A. Firsov, "Two-dimensional gas of massless Dirac fermions in graphene," Nature **438**(7065), 197–200 (2005).
23. S. Das Sarma, S. Adam, E. H. Hwang, and E. Rossi, "Electronic transport in two-dimensional graphene," Rev. Mod. Phys. **83**(2), 407–470 (2011).
24. A. H. Castro Neto, F. Guinea, N. M. R. Peres, K. S. Novoselov, and A. K. Geim, "The electronic properties of graphene," Rev. Mod. Phys. **81**(1), 109–162 (2009).
25. F. Keilmann and R. Hillenbrand, "Near-field microscopy by elastic light scattering from a tip," Philos. Trans. R. Soc., A **362**(1817), 787–805 (2004).
26. X. Chen, D. Hu, R. Mescall, G. You, D. N. Basov, Q. Dai, and M. Liu, "Modern Scattering-Type Scanning Near-Field Optical Microscopy for Advanced Material Research," Adv. Mater. **31**(24), 1804774 (2019).
27. O. Khatib, H. A. Bechtel, M. C. Martin, M. B. Raschke, and G. L. Carr, "Far Infrared Synchrotron Near-Field Nanoimaging and Nanospectroscopy," ACS Photonics **5**(7), 2773–2779 (2018).
28. I. D. Barcelos, H. A. Bechtel, C. J. S. de Matos, D. A. Bahamon, B. Kaestner, F. C. B. Maia, and R. O. Freitas, "Probing Polaritons in 2D Materials with Synchrotron Infrared Nanospectroscopy," Adv. Opt. Mater. **8**(5), 1901091 (2020).
29. S. C. Kehr, M. Cebula, O. Mieth, T. Härtling, J. Seidel, S. Grafström, L. M. Eng, S. Winnerl, D. Stehr, and M. Helm, "Anisotropy contrast in phonon-enhanced apertureless near-field microscopy using a free-electron laser," Phys. Rev. Lett. **100**, 1–4 (2008).

30. L. Wehmeier, T. Nörenberg, T. V. A. G. de Oliveira, J. M. Klopf, S.-Y. Yang, L. W. Martin, R. Ramesh, L. M. Eng, and S. C. Kehr, "Phonon-induced near-field resonances in multiferroic BiFeO$_3$ thin films at infrared and THz wavelengths," Appl. Phys. Lett. **116**(7), 071103 (2020).

31. T. V. A. G. de Oliveira, T. Nörenberg, G. Álvarez-Pérez, L. Wehmeier, J. Taboada-Gutiérrez, M. Obst, F. Hempel, E. J. H. Lee, J. M. Klopf, I. Errea, A. Y. Nikitin, S. C. Kehr, P. Alonso-González, and L. M. Eng, "Nanoscale-Confined Terahertz Polaritons in a van der Waals Crystal," Adv. Mater. **33**(2), 2005777 (2021).

32. B. Knoll and F. Keilmann, "Enhanced Dielectric Contrast in Scattering-Type Scanning Near-Field Optical Microscopy," Opt. Commun. **182**(4-6), 321–328 (2000).

33. H.-G. von Ribbeck, M. Brehm, D. W. van der Weide, S. Winnerl, O. Drachenko, M. Helm, and F. Keilmann, "Spectroscopic THz near-field microscope," Opt. Express **16**(5), 3430–3438 (2008).

34. K. Moon, H. Park, J. Kim, Y. Do, S. Lee, G. Lee, H. Kang, and H. Han, "Subsurface nanoimaging by broadband terahertz pulse near-field microscopy," Nano Lett. **15**(1), 549–552 (2015).

35. N. A. Aghamiri, F. Huth, A. J. Huber, A. Fali, R. Hillenbrand, and Y. Abate, "Hyperspectral time-domain terahertz nano-imaging," Opt. Express **27**(17), 24231 (2019).

36. X. Chen, X. Liu, X. Guo, S. Chen, H. Hu, E. Nikulina, X. Ye, Z. Yao, H. A. Bechtel, M. C. Martin, G. L. Carr, Q. Dai, S. Zhuang, Q. Hu, Y. Zhu, R. Hillenbrand, M. Liu, and G. You, "THz Near-Field Imaging of Extreme Subwavelength Metal Structures," ACS Photonics **7**(3), 687–694 (2020).

37. A. Pizzuto, D. M. Mittleman, and P. Klarskov, "Laser THz emission nanoscopy and THz nanoscopy," Opt. Express **28**(13), 18778 (2020).

38. A. Pizzuto, X. Chen, H. Hu, Q. Dai, M. Liu, and D. M. Mittleman, "Anomalous contrast in broadband THz near-field imaging of gold microstructures," Opt. Express **29**(10), 15190 (2021).

39. T. Kampfrath, K. Tanaka, and K. A. Nelson, "Resonant and nonresonant control over matter and light by intense terahertz transients," Nat. Photonics **7**(9), 680–690 (2013).

40. S. Kovalev, Z. Wang, J. Deinert, N. Awari, M. Chen, B. Green, S. Germanskiy, T. V. A. G. de Oliveira, J. S. Lee, A. Deac, D. Turchinovich, N. Stojanovic, S. Eisebitt, I. Radu, S. Bonetti, T. Kampfrath, and M. Gensch, "Selective THz control of magnetic order: new opportunities from superradiant undulator sources," J. Phys. D: Appl. Phys. **51**(11), 114007 (2018).

41. T. Jiang, V. Kravtsov, M. Tokman, A. Belyanin, and M. B. Raschke, "Ultrafast coherent nonlinear nanooptics and nanoimaging of graphene," Nat. Nanotechnol. **14**(9), 838–843 (2019).

42. H. Wang, L. Wang, and X. G. Xu, "Scattering-type scanning near-field optical microscopy with low-repetition-rate pulsed light source through phase-domain sampling," Nat. Commun. **7**(1), 13212 (2016).

43. H. T. Stinson, A. Sternbach, O. Najera, R. Jing, A. S. Mcleod, T. V. Slusar, A. Mueller, L. Anderegg, H. T. Kim, M. Rozenberg, and D. N. Basov, "Imaging the nanoscale phase separation in vanadium dioxide thin films at terahertz frequencies," Nat. Commun. **9**(1), 3604 (2018).

44. L. A. Walsh, A. J. Green, R. Addou, W. Nolting, C. R. Cormier, A. T. Barton, T. R. Mowll, R. Yue, N. Lu, J. Kim, M. J. Kim, V. P. LaBella, C. A. Ventrice, S. McDonnell, W. G. Vandenberghe, R. M. Wallace, A. Diebold, and C. L. Hinkle, "Fermi Level Manipulation through Native Doping in the Topological Insulator Bi 2 Se 3," ACS Nano **12**(6), 6310–6318 (2018).

45. F. Kuschewski, H.-G. von Ribbeck, J. Döring, S. Winnerl, L. M. Eng, and S. C. Kehr, "Narrow-band near-field nanoscopy in the spectral range from 1.3 to 8.5 THz," Appl. Phys. Lett. **108**(11), 113102 (2016).

46. F. Mooshammer, M. Plankl, T. Siday, M. Zizlsperger, F. Sandner, R. Vitalone, R. Jing, M. A. Huber, D. N. Basov, and R. Huber, "Quantitative terahertz emission nanoscopy with multiresonant near-field probes," Opt. Lett. **46**(15), 3572 (2021).

47. S. Düsterer, M. Rehders, A. Al-Shemmary, C. Behrens, G. Brenner, O. Brovko, M. Dellangela, M. Drescher, B. Faatz, J. Feldhaus, U. Frühling, N. Gerasimova, N. Gerken, C. Gerth, T. Golz, A. Grebentsov, E. Hass, K. Honkavaara, V. Kocharian, M. Kurka, T. Limberg, R. Mitzner, R. Moshammer, E. Plönjes, M. Richter, J. Rönsch-Schulenburg, A. Rudenko, H. Schlarb, B. Schmidt, A. Senftleben, E. A. Schneidmiller, B. Siemer, F. Sorgenfrei, A. A. Sorokin, N. Stojanovic, K. Tiedtke, R. Treusch, M. Vogt, M. Wieland, W. Wurth, S. Wesch, M. Yan, M. V. Yurkov, H. Zacharias, and S. Schreiber, "Development of experimental techniques for the characterization of ultrashort photon pulses of extreme ultraviolet free-electron lasers," Phys. Rev. Spec. Top.–Accel. Beams **17**(12), 120702 (2014).

48. Z. Wu, A. S. Fisher, J. Goodfellow, M. Fuchs, D. Daranciang, M. Hogan, H. Loos, and A. Lindenberg, "Intense terahertz pulses from SLAC electron beams using coherent transition radiation," Rev. Sci. Instrum. **84**(2), 022701 (2013).

49. A. Perucchi, S. Di Mitri, G. Penco, E. Allaria, and S. Lupi, "The TeraFERMI terahertz source at the seeded FERMI free-electron-laser facility," Rev. Sci. Instrum. **84**(2), 022702 (2013).

50. N. Adhlakha, P. Di Pietro, F. Piccirilli, P. Cinquegrana, S. Di Mitri, P. Sigalotti, S. Spampinati, M. Veronese, S. Lupi, and A. Perucchi, "The TeraFERMI Electro-Optic Sampling Set-Up for Fluence-Dependent Spectroscopic Measurements," Condens. Matter **5**(1), 8 (2020).

51. D. Daranciang, J. Goodfellow, M. Fuchs, H. Wen, S. Ghimire, D. A. Reis, H. Loos, A. S. Fisher, and A. M. Lindenberg, "Single-cycle terahertz pulses with >0.2 V/Å field amplitudes via coherent transition radiation," Appl. Phys. Lett. **99**(14), 141117 (2011).